

# PIV Measurements in Low Noise Optimized Air Jet Pump Demonstrators

Florin G. Florean, Andreea C. Petcu, Ionut Porumbel and Gabriel Dediu

**Abstract**— The paper presents experimental PIV measurements of axial and fluctuating velocity in a set of four air jet pump demonstrators of different geometries, including a baseline solution and three geometries that had been optimized from an acoustic standpoint by numerical simulations. The changes in the flow field introduced by the geometrical modifications of the jet pump with respect to the baseline solution are analyzed.

**Keywords**— PIV measurements, jet pump

## I. INTRODUCTION

**A**n ejector is a device which employs a high-velocity primary motive fluid to entrain and accelerate a slower moving secondary fluid. The resulting kinetic energy of the mixture is subsequently used for self-compression to a higher pressure, thus performing the function of a compressor. The ejector system has long been applied to jet pumps, vacuum pumps, high-altitude simulators, V/STOLs etc. Jet pumps have a lot of advantages, the most important being that they have no moving parts, resulting in wear resistance and lower production cost in comparison to other types of pump.

Ejector systems were also employed to reduce jet exhaust noise [1] and to enhance air-fuel turbulent mixing in many combustion engines [2, 3], in which the configuration of the ejector influences the whole performance of the system. A variety of configurations of the ejector system have been studied to improve the efficiency the ejector system employed. There are a number of geometrical and physical parameters that are still not well studied to date. The turbulent mixing, the

interaction between shock waves, boundary layers and shear layers and flow unsteadiness make the prediction of the flow field inside the ejector system extremely difficult.

Studies have been performed on jet pumps using computational fluid dynamics (CFD) and experimental techniques. Kim and Lee [4] carried out CFD numerical simulations of the flow in ejector-diffuser and studied the effect of the geometry on the entrained, secondary mass flow. Song et al. [5] studied the erosion intensity and distribution in the jet pump and the effect of the bent pipe on the erosion in the suction chamber. Lisowski and Momeni [6] presented CFD simulations of the flow phenomena appearing during the jet pump operation and assessed the influence of the modification of the motive nozzle on head pressure. Nanda et al. [7] presented two significant experimental results of the influence of the angle of placement and of the depth: at constant depth, the jet pump works better in the vertical position, but, as the depth is changing, inclined positions are better once the flow is commenced. Kandula and Kumar [8] show that small manufacturing errors in the nozzle plate holes result in a considerable change in the performance of the jet pump. A jet pump with multihole nozzle, having a smaller number of holes, with a smaller pitch circle diameter and a smaller mixing tube diameter yields higher efficiencies. Saker and Hassan [9] experimentally studied the characteristics of the jet pump. A simple geometry jet pump was designed, developed and tested. The experiments showed that stability must be considered between the suction head and the driving air mass flow rate. Miorini [10] focused on instantaneous phase averaged flow structures and associated turbulence in the passage of an axial water jet pump rotor using PIV measurements. Khodadadi and Vlachos [11] carried out studies of the turbulent mixing of a primary jet and its surrounding fluid in a pipe with inlet conditions that result in flow separation. Singh et al. [12] studied confined, swirling jets and it is observed that the introduction of swirl in the central jet enhances the merger, whereas higher swirl in the annulus enhances both mixing and flow development.

Recently, Gherman et al. [13] presented a numerical aerodynamic analysis of an air jet pump by means of RANS simulation, aiming at providing acoustically optimized solutions, without affecting the mixing and the efficiency. Also, Semlitsch et al. [14] conducted CFD simulations, using both RANS and LES approaches, of the turbulent flow in a jet

The work presented here was carried out under the European research project FP 7 Clean Sky “Optimization of air jet pump design for acoustic applications” – OPA, number 325977, financed by the European Commission. The authors also wish to thank the research team of LaVision GmbH, in Gottingen, Germany, for all their valuable help during the measurement campaign.

Florin G. Florean, is with the National Research and Development Institute for Gas Turbines COMOTI, Bucharest, 061126, Romania, (corresponding author - phone: (40) 72-373-5064; fax: (40) 21-434-0241; e-mail: florin.florean@comoti.ro).

Andreea C. Petcu is with the National Research and Development Institute for Gas Turbines COMOTI, Bucharest, 061126, Romania, (e-mail: andreea.petcu@comoti.ro).

Ionut Porumbel is with the National Research and Development Institute for Gas Turbines COMOTI, Bucharest, 061126, Romania, (e-mail: ionut.porumbel@comoti.ro).

Gabriel Dediu is with the National Research and Development Institute for Gas Turbines COMOTI, Bucharest, 061126, Romania, (e-mail: gabriel.dediu@comoti.ro).

pump consisting mainly of a convergent-divergent Venturi shaped duct where a primary stream is applied with the role of entraining a secondary jet.

The present paper presents PIV measurements of the mean and fluctuating velocity fields in several jet pump of different geometry. The constructive solutions of the jet pumps tested here represent the baseline and the optimized solutions provided by the numerical simulations carried out by Gherman et al. [13] and Semlitsch et al. [14].

## II. EXPERIMENTAL SETUP

### A. Demonstrators Geometry

The experimental results presented herein were carried out in four different geometrical configurations, materialized in four jet pump demonstrators. The first jet pump demonstrator reproduces the Baseline Solution (BS) geometry, presented in Fig. 1. The other three jet pump demonstrators were manufactured based on the geometries developed as a result of numerical optimization studies aimed at minimizing the noise produced by the jet pump [13].

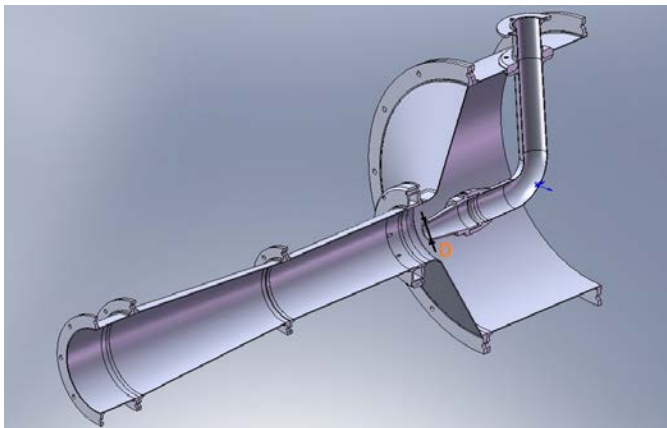


Figure 1. BS demonstrator geometry

The first jet pump demonstrator Optimized Solution (OS1) reproduces in general the baseline geometry with the exception of the primary nozzle jet exit, which, in this case, will be placed upstream of the baseline primary nozzle jet exit by two primary jet pipe nozzle diameters.

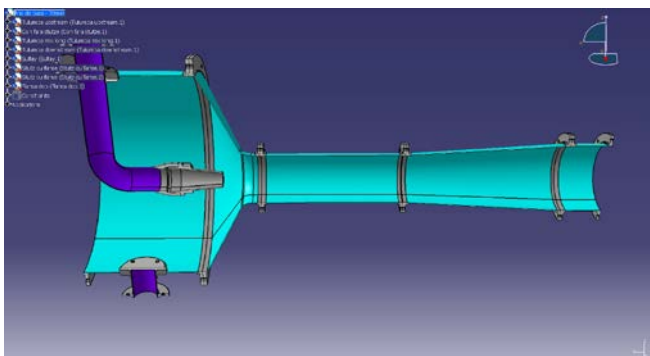


Figure 2. OS1 demonstrator geometry

This constructive solution was tested in two configurations: with a classic nozzle, as for the baseline case (OS1.1), and using 90° chevrons (OS1.2). The CAD model of OS1 is presented in Fig. 2.

The second selected solution uses the fluidic injection concept, applied on the same baseline body configuration. The solution uses eight injectors equally spaced on the jet pump casing, injecting the air at 25° with respect to the jet pump centreline. The CAD model of OS2 is presented in Fig. 3.

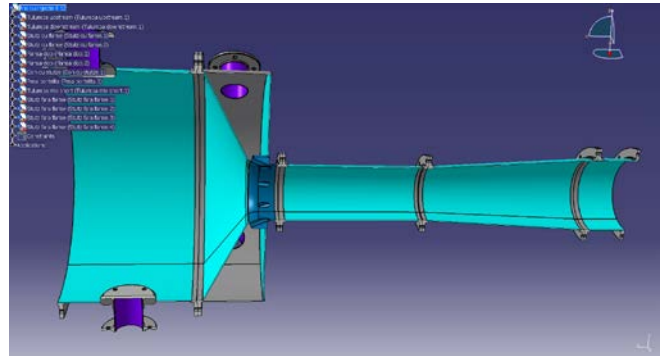


Figure 3. OS2 demonstrator geometry

In order to provide the optical access to the experimental zone in the mixing region for the PIV measurements presented here, the cylindrical segment where the mixing of the primary and secondary air stream is occurring was replaced by a quartz tube of the same diameter, as shown in Fig. 4.

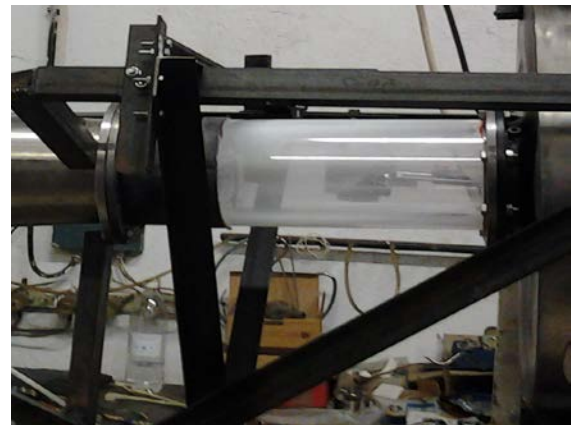


Figure 4. Optical access for PIV measurements

Since the quartz tube is not load bearing, a reinforcing system made up of several bars was designed, manufactured and installed in order to provide support for the demonstrator parts placed downstream of the experimental region, as shown in Fig. 4.

### B. Test Rig Instrumentation

The testing facilities existing at the Bucharest facilities of COMOTI were used to supply the primary air stream with the required parameters,  $p_1$  and  $T_1$  [15], both above the atmospheric conditions. The primary air is provided by the complex thermo- and gas dynamic testing facilities own by

COMOTI for experiments on liquid, gaseous, or biomass combustion, heat transfer studies and aviation or industrial turboengine testing. The testing facility is connected to a compressed air station, equipped with air filters, air dryers, air preheating installation, cooling towers and 2000 m<sup>3</sup> tanks, able to provide air up to Mach 3 and a pressure of maximum 16 bars.

The secondary air stream provided according to the specifications imposed by the project, with atmospheric pressure  $p_2$  and above atmospheric temperature  $T_2$  [15]. The secondary air is provided through a secondary air line, designed and manufactured by COMOTI.

The main objective of the presented aerodynamic testing campaign consists in instantaneous velocity measurements of the flow field in the optimized jet pump demonstrators. The velocity measurements were carried out through the stereo PIV method.

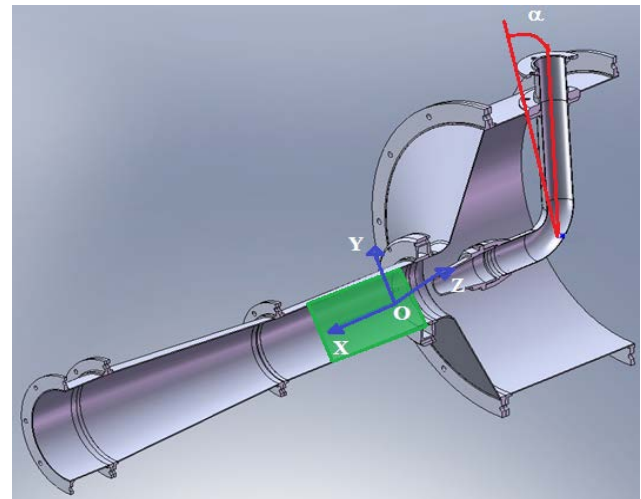
The method assumes the so-called seeding of the working fluid, meaning the insertion of solid particles in the flow. In this case, Titanium Oxide was used. The seeded flow was illuminated by an average intensity LASER beam, simultaneously emitted with the triggering of two fast cameras which record the image thus formed. Through the processing of these images, the displacement of the solid particles in the flow is determined, and, knowing the time interval between two snapshots, the velocity vector components were evaluated. The stereo PIV velocity measurements were carried out using maximum LASER power, a delay time between the LASER and the first camera triggering of 0.3689 ms, a time interval between the triggering of the two cameras of 10  $\mu$ s, a camera exposure time of 5  $\mu$ s for each camera, and a recording rate of 7.26 Hz. After the inlet thermodynamic parameters were achieved and stable, 10 sets of 100 double images were captured by the ICCD cameras for post-processing in order to provide the instantaneous velocity fields.

### C. Coordinate System

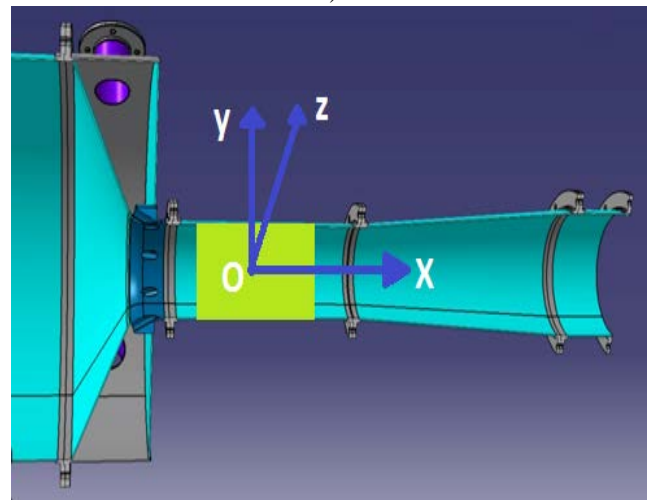
For all the geometrical configurations discussed earlier, the measurement field was a roughly rectangular domain placed in a horizontal plane along the demonstrators centrelines. Even though the measurement field was unchanged for all the presented experimental measurements with respect to the test rig due to the fixed position of the optical access segment shown in Fig. 4, its position varied with respect to each of the tested geometries. Thus, for BS and OS1, the normal direction to the measurement plane formed a 20° angle with the radial duct of the demonstrator's primary air stream, as shown in Fig. 5, where the measurement plane angle is denoted  $\alpha$  and the measurement plane is represented by the green rectangle.

For OS2, however, the measurement plane passes through two diametrically opposed primary air inlet holes, as shown in Fig. 5. As before, the measurement plane is represented by the green rectangle. The relative position of the measurement plane with respect to the primary air stream entry for all studied configurations is summarized in Fig. 6. For the purpose of the analysis presented in this paper, in this

measurement plane, the following coordinate system has been defined with respect to the overall demonstrator geometry. The orientation of the three axes is defined by the blue lines in Fig. 5, with the axial direction  $x$  along the demonstrators centrelines, the transversal direction  $y$  normal to the  $x$  axis in the measurement plane, and the spanwise direction  $z$  normal to the measurement plane, such that together the three axis form a Cartesian right coordinate system.



a)



b)

Figure 5. Measurement plane and coordinate system position

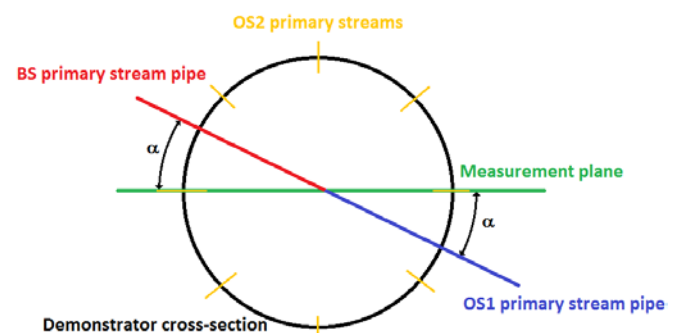


Figure 6. Measurement plane relative position with respect to the tested demonstrator geometries

The origin of the coordinate system is defined in the middle of the experimental plane, on the demonstrators' centerlines, at  $14.3 D$  from the demonstrator secondary inlet plane as shown in Fig. 7. Throughout the paper,  $D$  represents the BS primary air stream nozzle diameter, shown in Fig. 1.

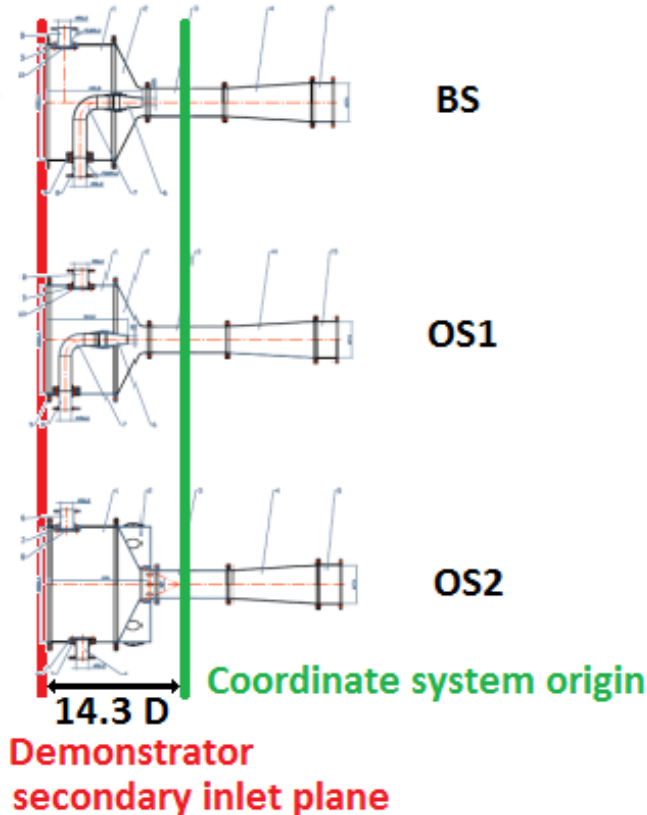


Figure 7. Coordinate system origin

### III. RESULTS

#### A. Mean Velocities

In the following, velocities are normalized by the numerically determined [13] primary jet velocity at the primary nozzle and the dimensions are normalized by  $D$ .

Figures 8, 9, respectively 10 present, for all the studied cases, the profiles of the three mean velocity components magnitude along the  $x$  axis at two positions along the  $y$  axis: on the centreline, and in the region of the shear layer delimiting the primary air stream jet, at a distance of  $1.1 D$  from the centerline [16] (the data at locations  $y = -1.1 D$  and  $y = 1.1 D$  mm was averaged).

The axial velocity on the centreline, shown in Figure 8, is the highest for BS, indicating the strongest primary jet. The reason is that the measurement plane is, in this case, the closest to the measurement section. From a noise production standpoint, which is the goal of the project, a strong primary jet is not desirable, and the results presented herein confirm that all the OSs improve on the BS geometry.

Among the OSs, the largest axial velocities on the centreline

are provided by OS2. The effect of the nozzle chevrons is found to be marginal, no significant overall differences being noticeable between OS1.1 and OS1.2.

In all cases, an acceleration of the flow in the axial direction at locations around the centreline can be noted. This is most likely an artefact of the experimental setup, due to unavoidable reflections present in the upstream region for all the measurements, caused by the deposition of seeding particles on the quartz tube that provided optical access to the measurement section, this deposition creating a mirror effect on the quartz tube, and, therefore, reflections. The effect was only appearing in the upstream section, and therefore, some experimental errors appear in this region in the data.

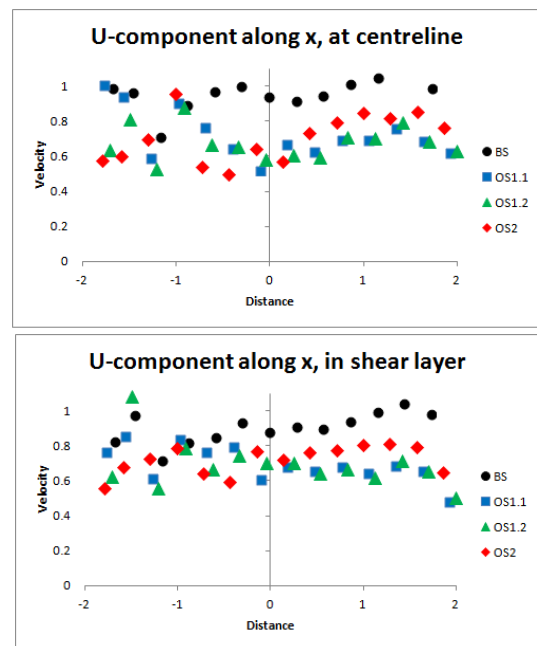


Figure 8. Axial mean velocity component along the  $x$  axis

Further downstream, at around  $x = 1.75 D$ , the axial velocity component decreases rapidly for all the studied cases, indicating the end of the primary jet potential core. The decrease starts sooner for OS2, at around  $x = 1.25 D$ , indicating a faster momentum transfer between the primary air streams and the entrained air. The improved momentum mixing observed for OS2 is an advantage from the noise production standpoint.

In the shear layer, in the upstream regions of the measurement section, the axial velocity component presents large fluctuations, indicating a very high turbulence level, such that the velocity fluctuations still show in the averaged data even after the averaging of 1000 instantaneous velocity snapshots. The high turbulence region is typical for a shear layer. The intensity of the fluctuations is higher for OS1.2, most likely an effect of the chevrons, which increase the turbulence level in the shear layer, and, henceforth, the momentum mixing. At around  $x = -10$  mm, the fluctuations tend to disappear, and the axial velocity remains roughly constant, its magnitude levels being ranked among the studied

cases in the same order as at the centreline: BS, OS2, OS1. The decrease in the axial velocity magnitude occurs faster at this transversal location, at around  $x = 1.5 D$  for BS and OS1, and again sooner, at  $x = 40 \text{ mm}$ , for OS2. It is important to note that the start of the axial deceleration of OS2 occurs at roughly the same axial location, at around  $x = 1 - 1.25 D$ , both at the centreline and in the shear layer, indicating that the tapering of the central air stream in this case is much smaller than in the other three cases, not typical for a circular round jet. This is reasonable, since for OS2 the primary air inlet occurs through eight circumferentially placed inclined nozzles that merge together in the central region, and not through a central axial nozzle, as in the other three presented cases. Therefore, the circular round jet spreading and decay laws [16] do not apply in this case.

The transversal velocity component on the centreline, presented in Fig. 9, indicates, for all cases, the presence of a stationary vortical structure in the flow field, causing the transversal oscillation of the flow with respect to the centreline. The vortex is the strongest of OS2, and the weakest for both OS1 cases. The presence of the vortex is an effect of the detachment of the boundary layer created on the demonstrator mixing segment and its entrainment by the main flow. This vortex is stronger in the OS2 case since the axial velocity gradients are higher here (large axial velocity over a thinner, lower spreading rate central region), due to the way the primary air enters the jet pump. For OS1, as the primary stream nozzle is further away from the measurement section, the axial velocity gradients are smaller, creating a less significant boundary layer detachment and a lower intensity vortex. The presence of the chevron in OS1.2 distorts the mean flow vortex, the shape of the transversal velocity profile in this case being less clearly indicating the mean flow vortex.

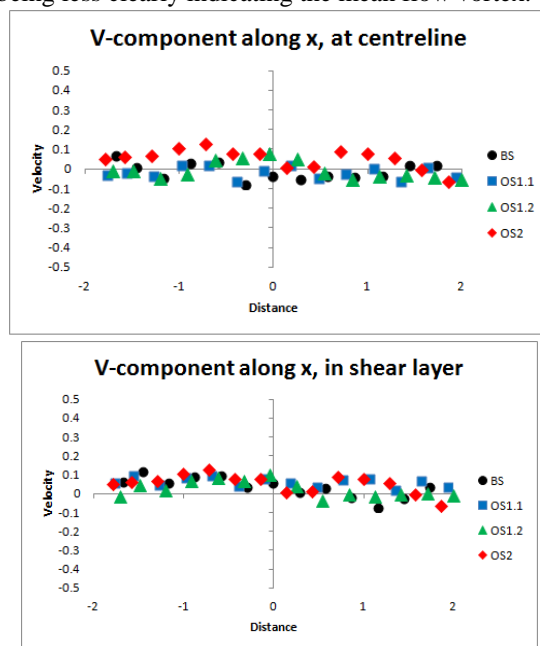


Figure 9. Transversal mean velocity component along the x axis

The same mean flow vortex can be observed, for all four cases, in the shear layer region, at  $y = 1.1 D$ . The intensity of the vortex is significantly lower than at the centreline due to the averaging process. As the flow is much more turbulent in the shear layer, the vortex kinetic energy is stored more in the smaller turbulent scales than in the mean flow. The magnitude of the mean transversal velocity is similar at this transversal location for all studied cases.

The situation is similar for the spanwise velocity component profile, presented in Fig. 10 at the centreline and in the shear layer. The shape of the mean flow vortex is less clear for this velocity component, due to the limitations of the planar PIV method, where the out-of-plane velocity component is evaluated based on the perspective provided by the two different angles made by the cameras with the flow, rather than directly measured [17, 18]. However, the ranking of the mean spanwise velocity component intensity remains the same as for the transversal velocity, highest for OS2 and lowest for OS1 at the centreline. In the shear layer region, the vortical movement of the flow is less well captured for all cases, the zero velocity level being slightly off for all cases.

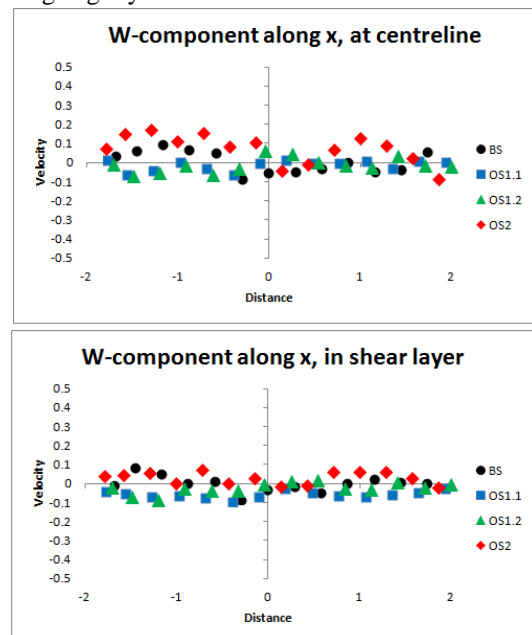


Figure 10. Spanwise mean velocity component along the x axis

Figures 11, 12, respectively 13 present, for all the studied cases, the profiles of the three mean velocity components magnitude along the y axis at positions along the x axis ranging from  $-D$  to  $D$ .

The axial velocity profile along the transversal direction is roughly parabolic for all the presented cases.

As shown in Fig. 11, For OS2, the parabolic profile is more significantly distorted, as an effect of the demonstrator geometry related to the primary air stream inlet.

The axial velocity is higher for the BS case, since the measurement section is the closest here to the primary jet nozzle exit. For all cases, the central, high velocity region of the flow expands towards downstream, due to the spreading of

the primary jet. The spreading rate is slightly larger for OS1, with only marginal differences between the two nozzle shapes, and the smallest for OS2.

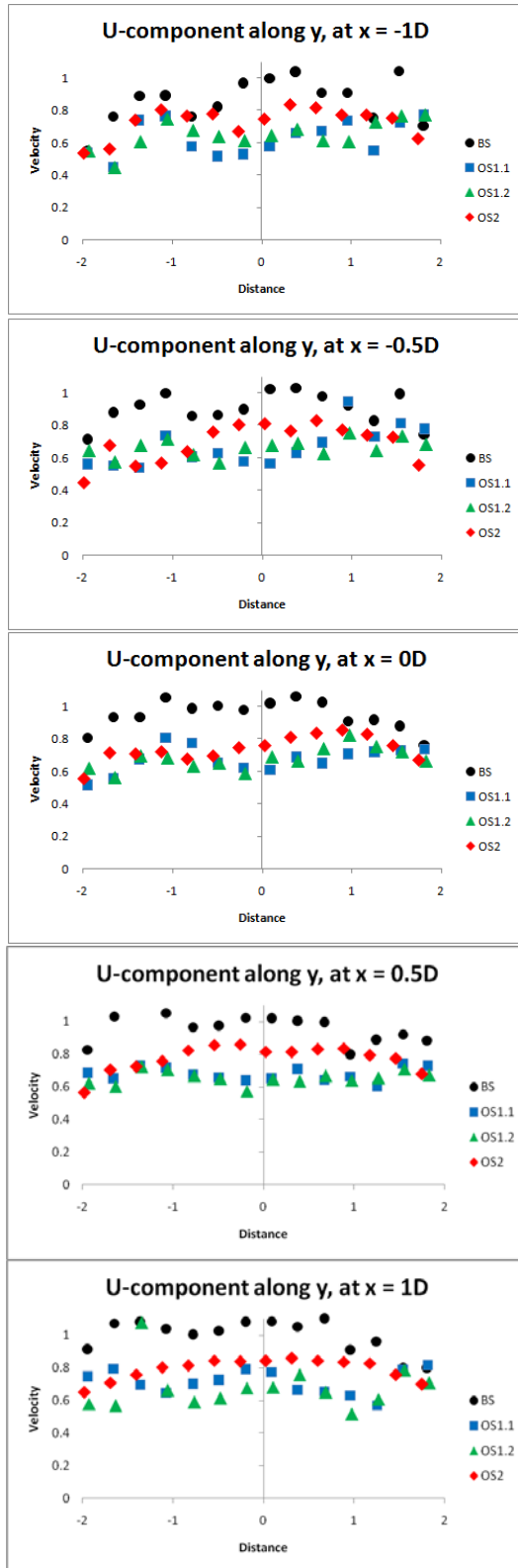


Figure 11. Axial mean velocity component along the y axis

A better view of the jet spreading rate, as illustrated by the

position of the shear layer, is shown in Fig.14.

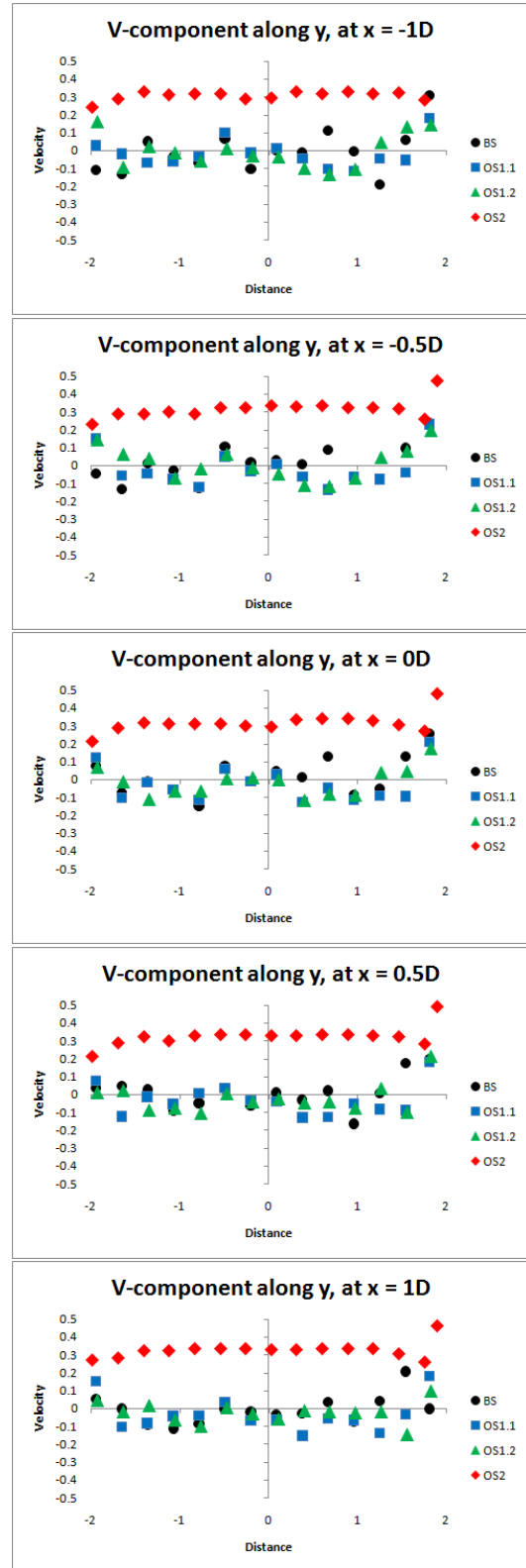


Figure 12. Transversal mean velocity component along the y axis

. Here, the position of the shear layer is defined, at each axial location, by the y-coordinate of the point where the transversal velocity gradient exceeds 10 % with respect to the

neighbouring measurement points. The positive and negative y-coordinates thus determined are averaged in Fig. 14.

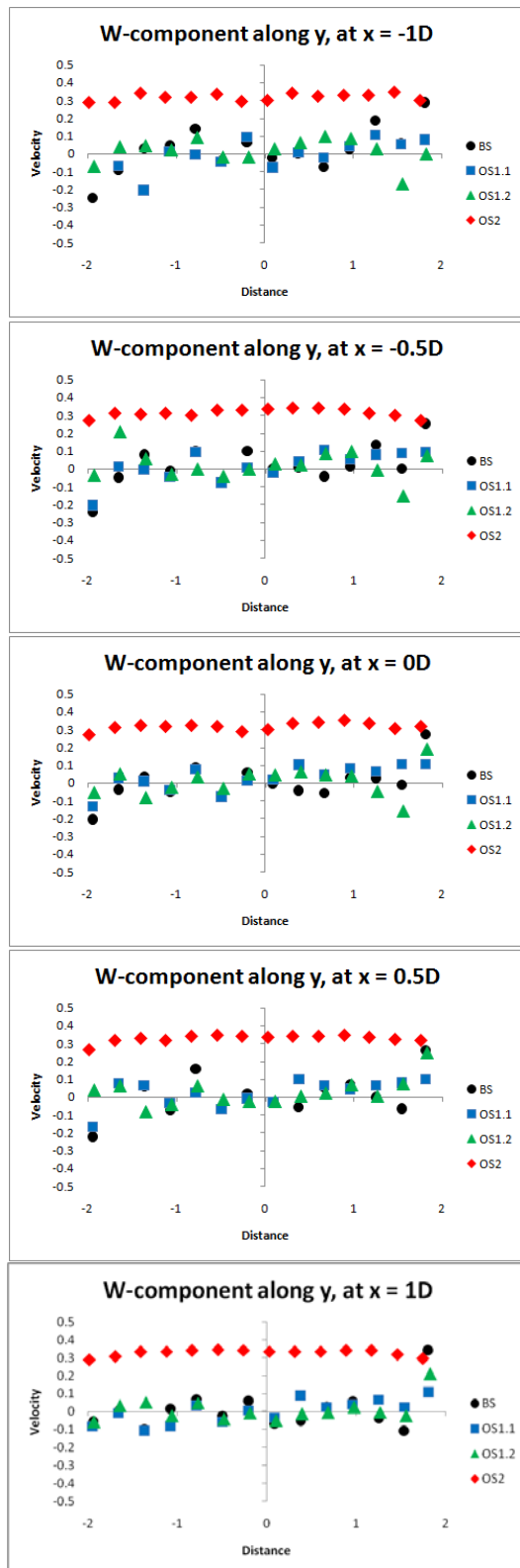


Figure 13. Spanwise mean velocity component along the y axis

The momentum mixing rate, illustrated by the axial velocity

gradient in the shear layer, away from the centreline, is roughly similar, with a slightly larger value registering for OS2. For BS, the transversal velocity profile along the y direction, presented in Fig. 12, exhibits a central region of very low transversal velocity, corresponding to the jet potential core, surrounded, first, by regions of positive velocity, corresponding to the jet spreading, away from the centreline, and next negative regions, corresponding to the entrainment of the surrounding air, towards the centreline.

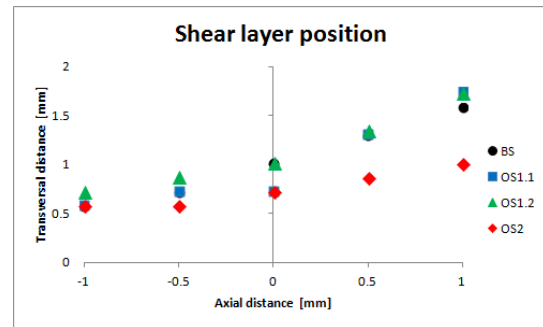


Figure 14. Shear layer position as defined by the decrease in the mean axial velocity

The intensity of both the positive and the negative velocities decreases downstream, following the jet spreading rate law of variation with the distance from the nozzle [16]. Similar profiles are also exhibited by both OS1 variants, with generally lower than the BS transversal velocity magnitudes in the positive velocity region, and higher than the BS transversal velocity magnitudes in the negative velocity region. This indicates that the transversal velocity corresponding to the jet spreading is slightly higher in the central region for the BS, where the jet nozzle is closer, while the jet entrainment is more significant for OS1, due to the optimized geometry. The effect of the chevrons is only visible in the far field, at  $x > 0$  where OS1.2 produces lower transversal velocities than OS1.1, due to the faster momentum mixing enabled by the chevrons. The OS2 transversal velocity has a different profile, with a negative velocity region close to the centreline and positive values away from it, reflecting the fact that the primary air enters at the jet pump casing, at a specified inclination, forming a ring shaped jet that progresses radially towards the centreline as it moves downstream. The behaviour of the spanwise velocity profiles, presented in Fig. 13 is very similar to the transversal velocity component profiles.

### B. Velocity Fluctuations

Figures 15, 16, respectively 17 present, for all the studied cases, the profiles of the three RMS fluctuating velocity components along the x axis at two positions along the y axis: on the centreline, and in the region of the shear layer delimiting the primary air stream jet, at  $y = 1.1 D$  (the data at locations  $y = -1.1 D$  and  $y = -1.1 D$  was averaged).

The axial velocity fluctuation profiles are uniform in the upstream region, particularly for BS and OS1, where only a minor increase towards downstream can be seen. Far

downstream outside of the jet, the turbulent fluctuation intensity decreases rapidly. For OS2, the axial velocity fluctuation profile presents an initial decay, followed by a sudden increase between 0 mm and D, and the final decrease, at the same rate with the other cases. The behaviour is consistent with the geometry of OS2, where a central, low velocity, low turbulence region can be expected in the near field, at axial location where the ring shaped jet did not yet reach the centreline.

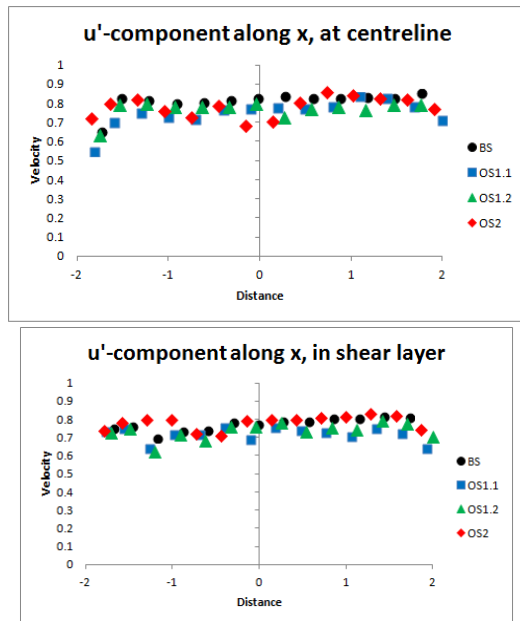


Figure 15. Axial RMS mean velocity component along the x axis

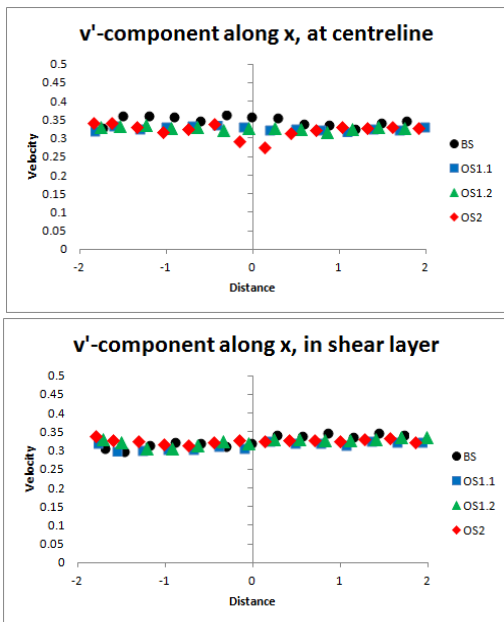


Figure 16. Transversal RMS mean velocity component along the x axis

Further downstream, as the ring edges reach the centreline, the turbulence intensity increases. Overall, OS1 has the lowest RMS velocity in the axial direction, with OS1.1 being the

lowest in the near field, and OS1.2 the lowest in the far field. In the low intensity regions around  $x = 0$ , OS 2 reaches the lowest RMS values.

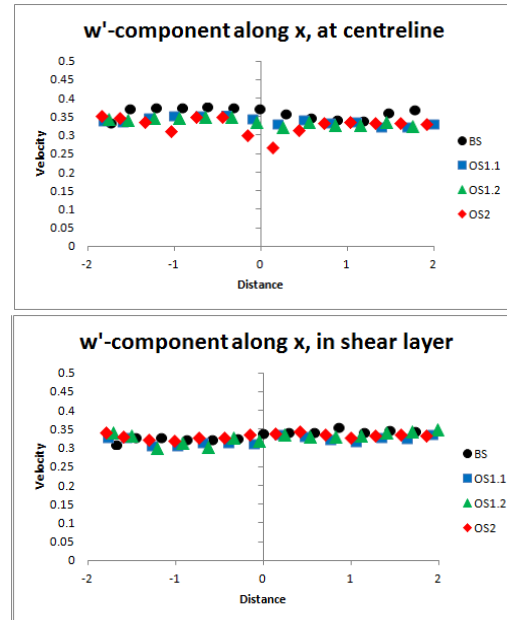


Figure 17. Transversal RMS mean velocity component along the x axis

In the shear layer region, all four profiles present a sudden increase, where the edge of the jet is crossed. For BS, this occurs at about  $x = -0.3 D$ , for OS1.1 at about  $x = 0.15 D$ , for OS 1.2 at about  $x = -0.4 D$  mm, and for OS2 at about  $x = -0.15 D$ . OS2 also presents a sudden decrease in the axial RMS velocity, at about  $x = -D$ , most likely indicating the crossing of the inner frontier of the ring shaped jet. The exit from the turbulent region of the shear layer triggers, far downstream, the decrease in the RMS fluctuation intensity.

In the transversal and spanwise directions, the RMS fluctuation profiles are similar. At the centreline, BS and OS1 present a low value upstream region, corresponding to the jet potential core, for both non-axial velocity components. The sudden increase in the velocity fluctuations for both components occurs first for BS, then for OS1.2, and last for OS1.1, indicating that the length of the potential core increases in the same order. As in the axial velocity fluctuation case, the OS2 RMS profiles show two peaks. Also for both components, the BS RMS values are the highest, while OS2 provides the lowest RMS intensity in regions close to  $x = 0$  mm. The situation repeats itself in the shear layer, for lower RMS intensities in all cases. The low RMS intensity region noticeable for OS2 is less important at this location, so OS1 provides the lowest RMS values in the upstream region, with insignificant differences between the two nozzle configurations.

Figures 18, 19, respectively 20 present, for all the studied cases, the profiles of the three RMS fluctuating velocity components along the y axis at positions along the x axis ranging from  $-D$  to  $D$ .

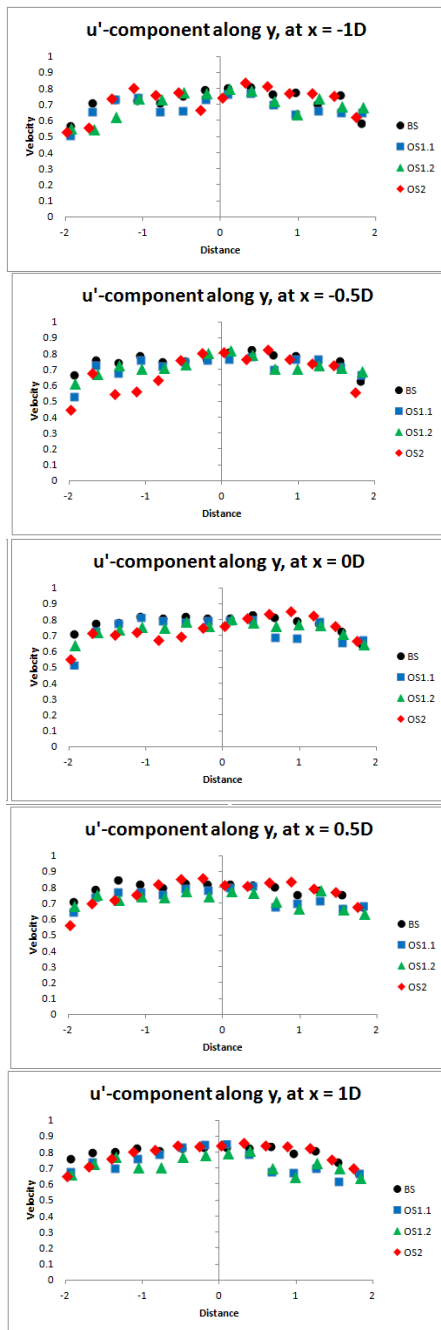


Figure 18. Axial RMS velocity component along the y axis

The BS and OS1 profiles present small peaks in the axial velocity RMS, corresponding to the two jet edges. The position of the peaks can be used, as shown in Fig. 21, to define the jet edges. The peaks were defined as having a value larger by at least 10 % when compared to the neighbouring axial RMS values. The width of the jet is found smaller than that defined by the peak axial velocity, presented in Fig. 14, but the width and spreading rate in the four analyzed cases is found in good correlation with that in Fig. 14.

The overall intensity of the axial RMS velocity is the largest for OS2, followed by BS, OS1.1 and OS1.2.

The transversal and spanwise RMS velocity components

present similar profiles, but at a reduced intensity. BS has, for these RMS velocity components the highest values, resulting in a turbulent field closer to isotropic, while the lowest components, resulting in the most anisotropic field, are found for OS2, particularly in the near field ( $x \leq 0$ ).

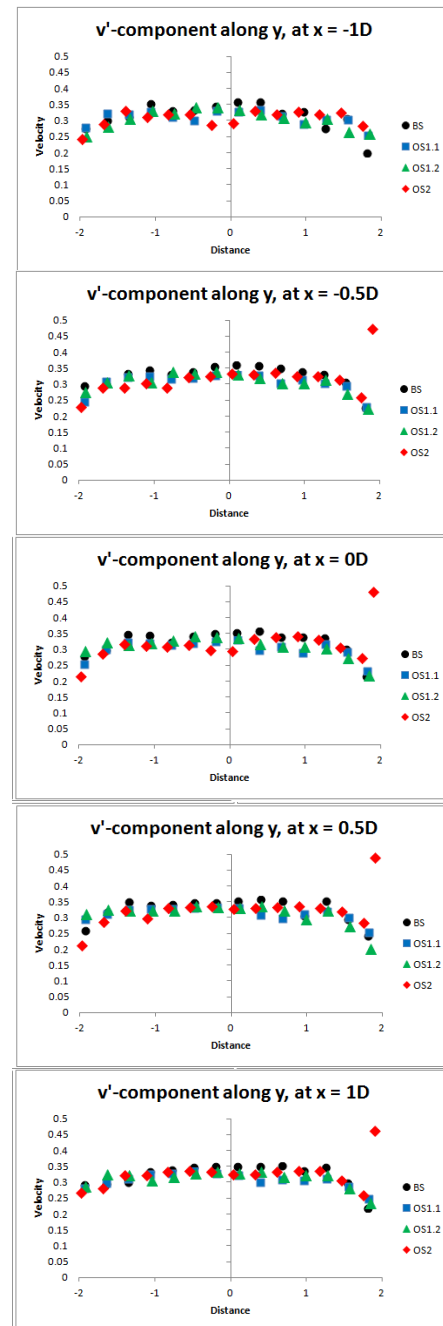


Figure 19. Transversal RMS velocity component along the y axis

#### IV. CONCLUSION

The analysis of the data gathered through PIV experimental measurements of the flow in the mixing region in the three optimized solution demonstrator geometries is carried out in this document.

The highest axial velocity component value on the

centreline is measured for BS, while the lowest is measured for OS1, due to the axial distance to the primary exhaust nozzle. The fastest momentum mixing between the primary stream and the entrained air is registered for OS2, which is an advantage from the noise production standpoint.

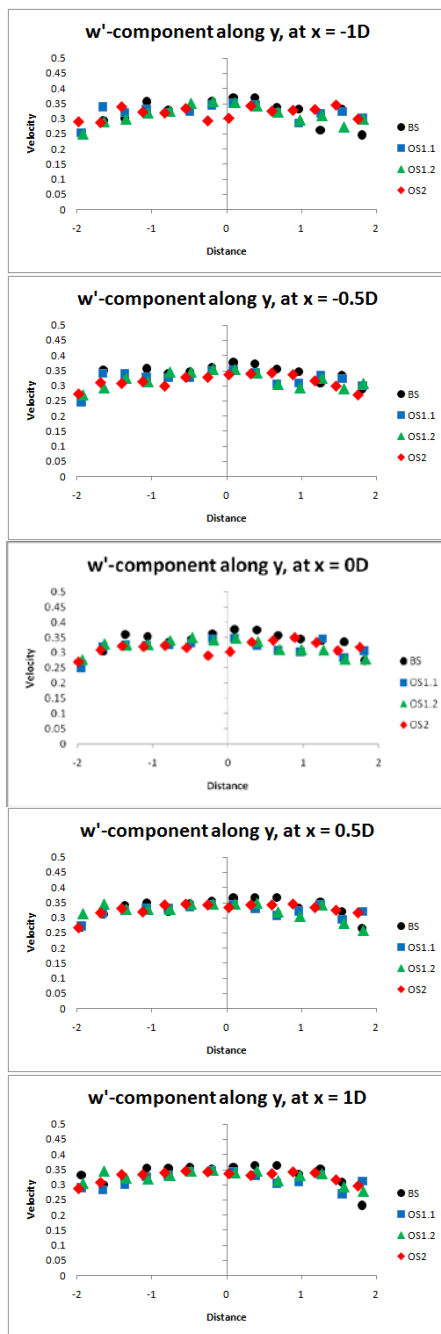


Figure 20. Spanwise RMS velocity component along the y axis

In the shear layer, large fluctuations of the mean axial velocity are observed, indicating a high level of turbulence in the region, with a maximum value noted for OS1.2, due to the presence of the chevrons. The tapering of the central air stream is found minimal for OS2, due to the configuration of the primary air inlet. Vortical structures are observed in the mean flow in the transversal and spanwise profiles, due to the

detachment of the boundary layer on the mixing segment duct. The vortex is the strongest of OS2, due to the higher axial velocity gradients, and the weakest for both OS1 cases.

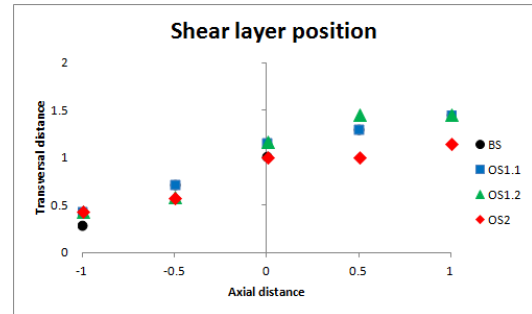


Figure 21. Shear layer position as defined by the peak in the RMS axial velocity

In the transversal direction, the axial velocity profile along the transversal direction is roughly parabolic for all the presented cases. The axial velocity is higher for the BS case, since the measurement section is the closest here to the primary jet nozzle exit. For all cases, the central, high velocity region of the flow expands towards downstream, due to the spreading of the primary jet. The spreading rate is slightly larger for OS1, with only marginal differences between the two nozzle shapes, and the smallest for OS2. The momentum mixing rate is roughly similar, with a slightly larger value registering for OS2. The transversal and spanwise velocity profiles indicate that the jet spreading is slightly higher in the central region for the BS, where the jet nozzle is closer, while the jet entrainment is more significant for OS1, due to the optimized geometry. The OS2 transversal and spanwise velocity profiles are different from the other cases, indicating a ring shaped jet that progresses radially towards the centreline as it moves downstream.

The axial velocity fluctuation profiles are uniform in the upstream region, while far downstream outside of the jet, the turbulent fluctuation intensity decreases rapidly. For OS2, the axial velocity fluctuation profile presents an initial decay, followed by a sudden increase and the final decrease, at the same rate with the other cases. Overall, OS1 has the lowest RMS velocity in the axial direction, with OS1.1 being the lowest in the near field, and OS1.2 the lowest in the far field. In the low intensity regions in the centre of the measurement field, OS 2 reaches the lowest RMS values.

In the shear layer region, all four profiles present a sudden increase, where the edge of the jet is crossed. The exit from the turbulent region of the shear layer triggers, far downstream, the decrease in the RMS fluctuation intensity.

In the transversal and spanwise directions, the RMS fluctuation profiles are similar. At the centreline, BS and OS1 present a low value upstream region, corresponding to the jet potential core, for both non-axial velocity components. The sudden increase in the velocity fluctuations for both components occurs first for BS, then for OS1.2, and last for OS1.1, indicating that the length of the potential core increases

in the same order. As in the axial velocity fluctuation case, the OS2 RMS profiles show two peaks. The BS RMS values are the highest, while OS2 provides the lowest RMS intensity in regions close to  $x = 0$ .

## REFERENCES

- [1] T. Z. Dong, R. R. Mankbadi, "Simulation of Un-steady Flow in Nozzle-Ejector Mixer," *Journal of Propulsion and Power*, Vol.15, No.4, 1999, pp.539-543.
- [2] W. E. Francis, M. L. Hoggarth, and J. J. Templeman, "The Design of Jet Pumps and Injectors for Gas Distribution and Combustion Purposes," *Proceedings of Symposium on Jet Pumps and Ejectors*, BHRA Fluid Engineering-Institution of Chemical Engineers, London, UK, No.6, 1972, pp.81-96.
- [3] C. F. Liu, F. Chen, "Analysis of Performance of the Second-Throat Ejector-Diffuser," *Journal of the Chinese Society of Mechanical Engineering*, Vol. 13, No.5, 1992, pp.478-482.
- [4] H. Kim, Y. Lee, "Numerical Simulation of the Supersonic Flows in the Second Throat Ejector Diffuser Systems", *Journal of Thermal Science*, Vol.8, No.4, 1999.
- [5] X. G. Song, H. J. Park, S. G. Kim, and Y. C. Park, „Performance Comparison and Erosion Prediction of Jet Pumps by Using a Numerical Method", *Mathematical and Computer Modelling*, Vol. 57, No. 1-2, 2013, pp. 245-253.
- [6] E. Lisowski and H. Momeni, „CFD Modelling of a Jet Pump with Circumferential Nozzles for Large Flow Rates", *Archives of Foundry Engineering*, Vol. 10, Special Issue 3, 2010, pp. 69-72.
- [7] R. Nanda, S. Gupta, and A. K. N. Shukla, " Experimental Setup for Performance Characterization of a Jet Pump with Varying Angles of Placement and Depth", *Journal of Petroleum Exploration, Production and Technology*, Vol. 1, 2011, pp.107–110.
- [8] J. Kandula, M. V. Kumar, "Experimental Analysis on Multi Hole Nozzle Jet Pump", *International Journal of Modern Engineering Research*, Vol. 3, No. 1, Jan-Feb. 2013, pp-193-198.
- [9] A. A. Saker, H. Z. Hassan, "Study of the Different Factors that Influence Jet Pump Performance", *Open Journal of Fluid Dynamics* [online journal], Vol. 3, 2013, pp. 44-49. Available: <http://dx.doi.org/10.4236/ojfd.2013.32006>
- [10] R. Miorini, "Investigation on the Flow Inside Pumps by Means of 2D Particle Image Velocimetry", Ph.D. dissertation, Facoltà di Ingegneria Dipartimento di Ingegneria Industriale, Università degli Studi di Bergamo, 2010.
- [11] J. M. Khodadadi and N. S. Vlachos, "Experimental and Numerical Study of Confined Coaxial Turbulent Jets", *AIAA Journal*, Vol. 27, No. 5, May 1989.
- [12] S. N. Singh, D. P. Agrawal, R. C. Malborta, and A. K. Raghava, „Mean-Velocity Distributions of Contra-Swirling Coaxial, Confined Jets", *Experiments in Fluids*, Vol. 7, No. 7, January 1989, pp. 501-504.
- [13] B. G. Gherman, I. Malael, M. Mihaescu, and I. Porumbel, "Jet Pump Optimization through Reynolds Averaged Navier-Stokes Simulation Analysis", *AIAA 22<sup>nd</sup> Computational Fluid Dynamics Conference*, Dallas, TX, USA, 2015.
- [14] B. Semlitsch, E. Laurendeau, and M. Mihaescu, "Steady-State and Unsteady Simulations of a High Velocity Jet into a Venturi Shaped Pipe", *Proceedings of the 4<sup>th</sup> Joint US-European Fluids Engineering Summer Meeting*, FEDSM 2014, August 3-7, 2014, Chicago, IL, USA, FEDSM2014-22162.
- [15] Liebherr Aerospace, "Technical Report", T-JTI-ACOUST-SP-0002, 22.04.2013, unpublished
- [16] S. B. Pope, "Turbulent Flows", Cambridge University Press, UK, 2000
- [17] LaVision GmbH, Flow Master, Product Manual, Gottingen, Germany, 2007
- [18] LaVision GmbH, DaVis 7.2 Software, Product Manual, Gottingen, Germany, 2008